Materials Science & Engineering A 662 (2016) 443–455

Contents lists available at ScienceDirect

Materials Science & Engineering A

journal homepage: www.elsevier.com/locate/msea

Tempering behavior of a low nitrogen boron-added 9%Cr steel

I. Fedorova [a,b,*], A. Kostka [b,c], E. Tkachev [a], A. Belyakov [a], R. Kaibyshev [a]

[a] Belgorod State University, 308015 Belgorod, Russia
[b] Max-Planck-Institut fur Eisenforschung GmbH, 40237 Dusseldorf, Germany
[c] Institut fur Werkstoffe, Ruhr-Universitat Bochum, 44801 Bochum, Germany

ARTICLE INFO

Article history:
Received 12 December 2015
Accepted 21 March 2016
Available online 22 March 2016

Keywords:
Mechanical characterization
Electron microscopy
Creep resistant steel
Phase transformation
Precipitation
Chromium rich films
Tempered martensite
Fracture

ABSTRACT

The effect of tempering temperature on microstructure and mechanical properties was studied in a low-nitrogen, high-boron, 9%Cr steel. After normalizing and low-temperature tempering, cementite platelets precipitated within the martensitic matrix. This phase transformation has no distinct effect on mechanical properties. After tempering at 500 °C, $M_{23}C_6$ carbides appeared in the form of layers and particles with irregular shapes along the high-angle boundaries. Approximately, 6% of the retained austenite was observed after normalizing, which reduced to 2% after tempering at 550 °C. This is accompanied by reduction in toughness from 40 J/cm^2 to 8.5 J/cm^2. Further increase of the tempering temperature led to spheroidization and coagulation of $M_{23}C_6$ particles that is followed by a significant increase in toughness to 250 J/cm^2 at 750 °C. Three-phase separations of M(C,N) carbonitrides to particles enriched with V, Nb and Ti were detected after high-temperature tempering.

1. Introduction

High-chromium creep-resistant martensitic steels are widely used for critical components of fossil power plants that operate at temperatures up to 620 °C [1,2]. Unfortunately, these steels are affected by a breakdown of creep strength during long-term service, which is associated with the formation of coarse Z-phase particles at the expense of nanoscale M(C,N) carbonitrides [1,3–9]. Z-phase is a thermodynamically stable nitride that contains primarily Cr and V [5–7]. Because carbon cannot replace nitrogen in the Z-phase [5–7], the breakdown in long-term creep strength of 9–12%Cr martensitic steels is suppressed or shifted to longer rupture times by lowering nitrogen content. Recently, an advanced 9Cr-3W-3Co steel that exhibits superior creep strength with low nitrogen and high boron content was developed for 650 °C ultra-super-critical (USC) plants [1,9–15]. In addition, this type of 9%Cr steel has an enhanced long-term creep strength in welded joints, where type IV failure is suppressed [10–12,15]. Boron replaces carbon in $M_{23}C_6$ carbides, i.e., it forms a $M_{23}(B,C)_6$ phase, which is more resistant to coarsening under creep conditions than the B-free carbides [1,13,15]. However, high boron concentrations lead to embrittlement due to the formation of coarse BN particles or segregation to boundaries [16–18]. Moreover, the precipitation of BN phase decreases the amount of effective boron and nitrogen in $M_{23}C_6$ carbides and M(C,N) carbonitrides, respectively. This reduces the fraction of carbonitrides and rises the coarsening rate and, therefore, results in creep resistance degradation [10]. A BN-free microstructure is achieved by balancing the N+B content according to a BN solubility diagram in 9–12%Cr steels or by high-temperature annealing that dissolves these nitrides into an austenitic matrix [9,16–18]. The absorption of ~0.05 wt%N in 9–12%C steels occurs during the electric arc furnace melting followed by air casting [1]. The use of vacuum degassing equipment or vacuum induction melting (VIM) allows one to decrease the N content down to 0.01 or 0.002 wt%, respectively, and produces the high B 9–12%Cr steels, which are not susceptible to embrittlement [1]. For instance, no BN particles were found in a10%Cr steel that contained 30 ppm of N and 80 ppm of B [19].

Normally, the heat treatment process for 9–12%Cr steels consists of normalizing and tempering followed by air cooling [1]. After normalizing, the structure is martensitic [20] and BN particles may precipitate at boundaries of prior austenite grains (PAG) or packets [16]. During tempering, a number of different carbides precipitate, and many of them are metastable phases at lower temperatures [1,19,21]. The thermodynamically stable $M_{23}C_6$-type carbides and M(C,N) carbonitrides precipitate at the boundaries of PAGs, packets, blocks and martensitic laths and within the martensitic matrix after tempering at temperatures that range from 750 to 780 °C [1,22]. This dispersion of secondary phase particles plays a key role in superior creep strength of 9–12%Cr steels [1–

* Correspondence to: Technical University of Denmark Produktionstorvet, building 425, 2800 Kgs., Lyngby, Denmark.
E-mail address: irfe@mek.dtu.dk (I. Fedorova).

http://dx.doi.org/10.1016/j.msea.2016.03.092
0921-5093/

3,26,27–29]. The increase in the B content and the decrease in the N content significantly affect precipitation sequences during tempering, i.e., the chemical composition, morphology and distribution of particles in the transition and equilibrium phases [19,21]. Therefore, it is important to understand the precipitation behavior of different types of dispersoids in modern steels because they can easily nucleate. Some dispersoids stabilize the tempered martensite lath structure (TMLS) under service conditions. However, tempered martensite embrittlement takes place after tempering at ~500 °C, or long-term embrittlement occurs at approximately 600 °C service temperature [1,15,20–29]. The shape, size distribution, origin and nature of second-phase particles in TMLS significantly affect the creep resistance of 9–12%Cr steels [1–11,21,22–29]. The morphological characteristics and structural parameters of martensite depend on the tempering temperature and are also important for the creep strength [1,13,19,21–30]. Thus, the main goal of this study is to correlate the tempering effect with the microstructure and properties of a low nitrogen boron-added 9%Cr steel. Specific emphasis is put on the tempering temperature effect on the characteristics of martensite structure and the dispersion of secondary phase particles. The mechanical properties, especially the impact toughness of 9–11% Cr steels, significantly depend on tempering conditions [13,20,31,32]. Therefore, the second objective is to study the dependence of hardness, tensile properties and toughness on the tempering temperature.

2. Experimental procedure

The high-B and low N-steel with a chemical composition shown in Table 1 was produced using VIM followed by solution treatment at 1150 °C and hot forging at temperatures of 1150–1000 °C. Next, the billets were normalized at 1060 °C for 30 min followed by air cooling. Tempering was performed for 3 h at temperatures that ranged from 350 to 780 °C. Hardness measurements were performed using a Wolpert 3000 BLD device at ambient temperature. Charpy impact tests were performed at an ambient temperature on standard $10\times10\times55\ mm^3$ specimens with a 2 mm V-notch according to ASTM E23-05 using an Instron IMP460 machine with a 300 J capacity. Two types of tension tests were performed using an Instron 5882 testing machine at a strain rate of $2\times10^{-3}\ s^{-1}$. The specimens had a $1.4\times3\ mm^2$ cross-section and a 16 mm gauge length. First, the samples that were tempered at different temperatures were tested at the same tempered temperatures. Second, the samples tempered at different temperatures were tensioned at room temperature. Differential scanning calorimetry (DSC) was performed using an SDT Q600 (TA Instruments) calorimeter on ~45 mg specimens during heating from an ambient temperature to 1100 °C at a rate of 20 °C min^{-1} and cooling in an argon atmosphere at the same rate.

Structural characterization was performed using a JEM-2100 transmission electron microscope (TEM) equipped with an INCA energy-dispersive X-ray spectrometer (EDS) and a Quanta 600 FEG scanning electron microscope incorporating an orientation imaging microscopy (OIM) system. The TEM foils were prepared using the double jet electro-polishing method with a 10% solution of perchloric acid in glacial acetic acid and an application of voltage of 25 V at room temperature. The transverse lath/subgrain sizes were measured on the TEM micrographs using a linear intercept method by counting all clearly visible sub-boundaries. The dislocation density was estimated by counting individual dislocations in lath/subgrain interiors on at least six arbitrary selected typical TEM images [33]. The precipitates were identified using both the chemical analysis and the selected area diffraction method by extracting carbon replicas. The size distribution of the secondary phase particles was estimated by counting from 150 to 250 particles per specimen on at least 15 arbitrarily selected typical TEM images for each data point.

The equilibrium mole fractions of phases and their chemical composition were calculated with the Thermocalc software using the TCFE7 database. Austenite, ferrite, cementite (Fe_3C), carbides ($M_{23}C_6$, M_7C_3, M_6C), carbonitrides (M(C,N)), Laves phase, and BN phases were independently chosen for the analysis. The chemical composition and volume fraction of thermodynamically metastable phases were calculated using the suspension of equilibrium phases.

3. Results

3.1. Thermodynamic calculations of phase equilibrium

The temperature effect on the calculated mole fractions of thermodynamically stable phases, such as MX carbonitrides, Laves phase and $M_{23}C_6$ carbides, is shown in Fig. 1. Table 2 summarizes the chemical composition of these phases at different temperatures. It is seen that Thermo-Calc predicts an unusual precipitation sequence (Tables 2 and 3) that can be represented as follows:

$$\text{Martensite}\rightarrow M_3C+M_3B+M_6C\rightarrow M_{23}C_6+M_{23}(C,B)_6 \quad (1)$$

Both thermodynamically stable $M_{23}C_6$ carbide and transition cementite separate from martensite during tempering [12] and form the boron-free (M_3C and $M_{23}C_6$), boron-enriched ($M_3(C,B)$ and $M_{23}(C,B)_6$) phases (Tables 2 and 3). The $M_{23}C_6$ carbides contain a high fraction of Mo+W. The Mo/W ratio decreases from 20 to 0.5 with a temperature increase from 20 °C to 750 °C. The $M_{23}(C,B)_6$ phase is free from W and Mo. It is surprising that the M_3B and $M_{23}(C,B)_6$ phases are enriched with Fe, while the M_3B phase contains ~90 wt%Cr and no carbon. Both boron-containing phases, $M_{23}(C,B)_6$ and $M_3(C,B)$, constitute 25% of the overall amount of $M_{23}(C,B)_6/M_3(C,B)$ phases. Both types of cementite are free from W and Mo. Therefore, the precipitation of third meta-stable W-enriched M_6C carbide is predicted as a precursor phase for $M_{23}C_6$ carbides.

Two types of M(C,N) carbonitrides precipitate: Nb-C-enriched M(C,N) and V-N-enriched M(C,N) [1,21,34]. Increase of the tempering temperature leads to an increase of V and N concentrations in Nb-and C-enriched M(C,N) carbonitrides, respectively, and of Nb and C in V- and N-enrichedM(C,N) carbonitrides, respectively. However, even at 750 °C, the difference in chemical composition between the two types of M(C,N) carbonitrides is significant. The overall mole fraction of M(C,N) carbonitrides in the present steel is four-fold lower than in the steel with a conventional N content (0.05 wt%). This is primarily attributed to the decreased amount of V- and N-enriched M(C,N) carbonitrides[35].

At the normalizing temperature (1060 °C), the relatively high fractions of Nb-enriched M(C,N) carbonitrides and $M_{23}(C,B)_6$ phase

Table 1
Chemical composition (wt%) of the low nitrogen high boron 9% Cr steel investigated in this study.

C	Si	Mn	Cr	W	Mo	Nb	V	Co	Ni	Cu	Ti	Al	N	B
0.1	0.12	0.4	9	1.5	0.57	0.05	0.2	2.8	0.24	0.027	0.002	0.01	0.007	0.012

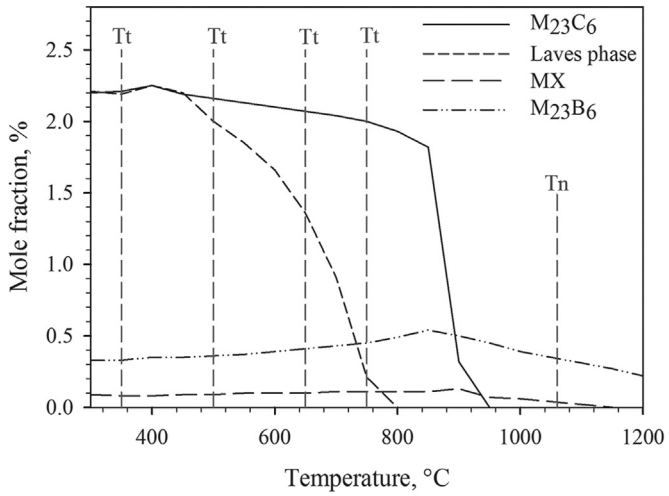

Fig. 1. Equilibrium mole fractions of phases at different temperatures calculated by Thermocalc. The experimental tempering temperatures are shown with dashed lines.

Table 3
The fractions of meta-stable phases calculated by Thermo-Calc.

Chemical Comp., wt%		Tempering temperature, °C					
		Room temperature	350		500		
M_3C	Mole fraction, %	0.56	0.27	0.74	0.27	0.84	0.27
	Fe	< 0.01	93.84	0.83	90.99	3.50	89.45
	Cr	92.81	0.10	91.16	2.57	87.71	3.56
	C	7.15	< 0.01	7.14	< 0.01	7.11	< 0.01
	B	< 0.01	6.06	< 0.01	6.06	< 0.01	6.05
	W	< 0.01	< 0.01	0.14	0.13	0.53	0.56
	Mo	< 0.01	< 0.01	< 0.01	0.25	0.02	0.38
	Co	< 0.01	< 0.01	< 0.01	< 0.01	0.02	< 0.01
M_6C	Mole fraction, %	1.29	0.77	1.97		1.79	
	Fe	17.38	18.56	17.70		19.11	
	W	70.10	34.24	56.95		56.37	
	Mo	3.39	44.43	17.40		16.46	
	C	1.75	2.00	1.83		1.85	

remain undissolved (Table 2). It is apparent that the increase in temperature from 750 to 1060 °C, which is accompanied by the $\alpha \rightarrow \gamma$ transformation, has no effect on the volume fraction of Nb-enriched M(C,N) carbonitrides and slightly decreases the $M_{23}(C,B)_6$ phase fraction. At 1060 °C, the $M_{23}(C,B)_6$ phase is highly enriched with Fe (Fe/Cr~2.1).

The austenite formation onset temperature, A_{c1}, and the transformation offset temperature, A_{c3}, were determined to be 858 and 902 °C, respectively. The BN phase formation was not anticipated for the entire range of simulated temperatures.

The formation of δ-ferrite during solidification and the subsequent solution treatment reduces the strength, ductility and toughness of 9–12%Cr heat-resistant steels and, therefore, must be avoided [1,36,37]. The Cr equivalent value, Cr_{eq}, is commonly used as a measure of susceptibility of high-chromium steels that contain additional elements, such as Si, Nb, V, Mo, W, N, to retain δ-ferrite during austenization. There is a significant difference in equations that have been proposed by different authors for calculating Cr_{eq} [1,30,38]. Currently, the most adopted version for this expression is as follows [1]:

$$Cr_{eq} = Cr + 6Si + 4Mo + 1 \cdot 5W + 11V + 5Nb - 40C - 30N - 4Ni - 2Mn - 2Co \quad \text{(in wt\%)} \qquad (2)$$

In the studied system, $Cr_{eq} = 5.13$ and, thus, δ-ferrite is not present ($Cr_{eq} \leq 10$) and, therefore, the 9%Cr steel is not susceptible to the formation of δ-ferrite.

Table 2
Equilibrium mole fractions of thermodynamically stable phases calculated by Thermo-Calc.

Chemical comp., wt%		Tempering temperature, °C										
		Room temperature		350		500		650		750		1060
MX	Mole fraction, %	0.14		0.08		0.09		0.10		0.11		0.04
		0.07	0.07	0.06	0.02	0.05	0.04	0.06	0.04	0.07	0.04	
	Nb	< 0.01	89.87	3.60	89.20	9.98	86.91	83.66	14.40	80.73	18.488	86.15
	V	85.64	< 0.01	79.81	0.10	72.78	1.23	2.77	67.44	4.013	62.581	0.96
	Cr	< 0.01	< 0.01	< 0.01	0.07	0.08	0.41	1.58	0.41	2.835	1.017	0.95
	C	< 0.01	10.13	< 0.01	9.07	0.22	7.81	7.88	0.95	7.825	1.665	8.67
	N	14.36	< 0.01	16.53	1.56	16.90	3.64	4.11	16.72	4.542	16.121	2.83
Laves phase	Mole fraction, %	2.22		2.19		2.00		1.36		0.21		–
	W	53.99		54.03		54.84		54.88		54.90		
	Fe	35.79		31.29		31.53		33.28		34.07		
	Cr	3.98		8.34		7.89		6.16		5.36		
	Mo	6.18		5.21		4.99		5.25		5.27		
	Nb	0.05		1.13		0.73		0.34		0.25		
	Co	< 0.01		< 0.01		0.03		0.08		0.14		
$M_{23}C_6$	Mole fraction, %	2.44		2.55		2.52		2,48		2.45		0.34
		2.11	0.33	2.21	0.34	2.16	0.36	2.07	0.41	2.00	0.45	
	Cr	66.59	89.11	68.99	72.07	67.56	62.57	61.22	50.57	53.08	44.24	30.43
	Fe	0.01	5.77	1.71	22.85	4.51	32.34	11.31	44.29	17.83	50.54	64.28
	B	< 0.01	5.12	< 0.01	4.89	< 0.01	4.54	< 0.01	3.96	< 0.01	3.54	3.97
	C	5.16	< 0.01	5.15	0.19	5.14	0.54	5.02	1.13	4.82	1.57	1.04
	W	< 0.01	< 0.01	0.01	< 0.01	1.01	< 0.01	6.68	< 0.01	14.76	< 0.01	< 0.01
	Mo	20.59	< 0.01	20.35	< 0.01	18.92	< 0.01	13.45	< 0.01	7.32	< 0.01	< 0.01
	Co	< 0.01	< 0.01	< 0.01	< 0.01	< 0.01	< 0.01	< 0.01	< 0.01	0.01	0.01	0.24

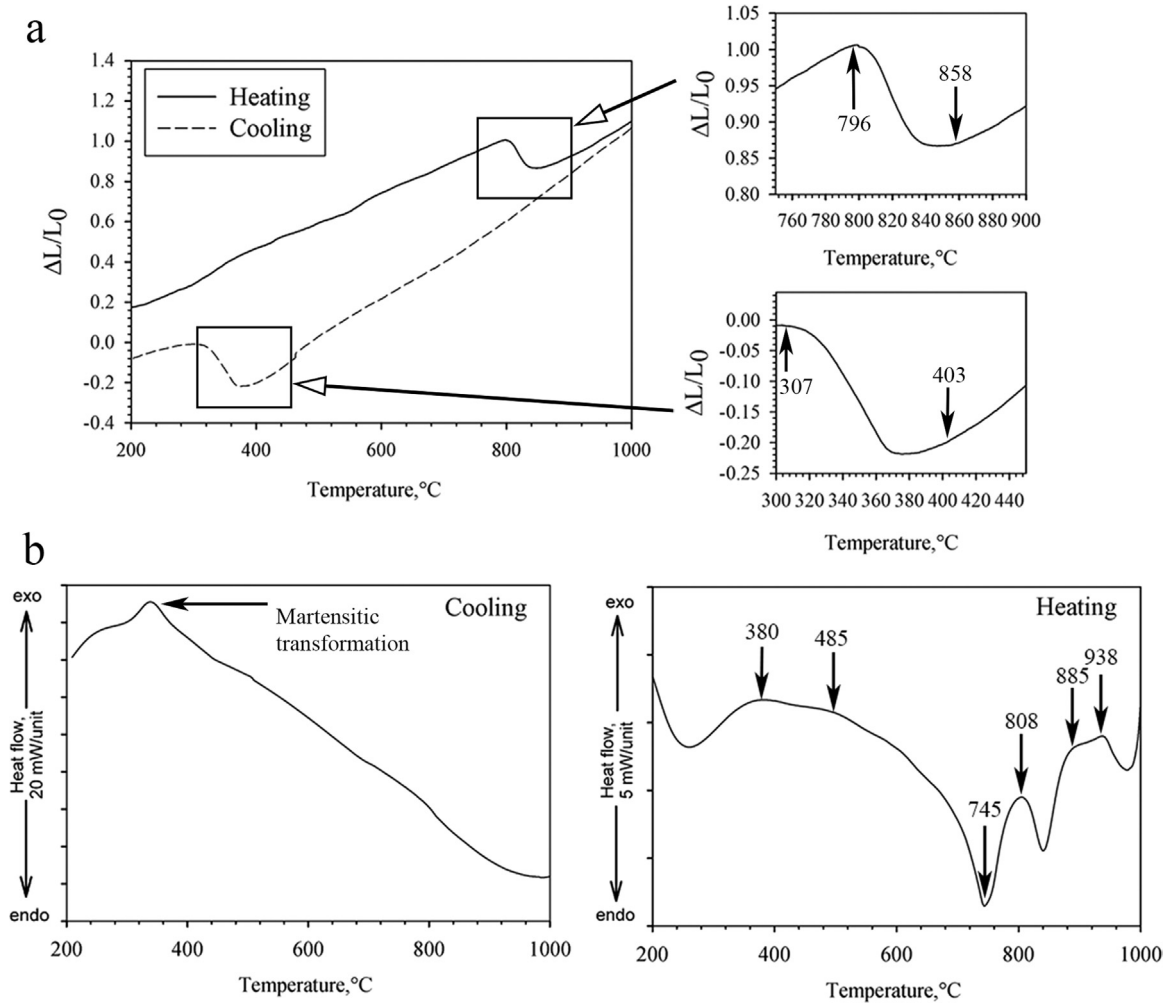

Fig. 2. Expansion (a) and DSC (b) curves of the low nitrogen martensitic steel.

3.2. DSC dilatometric analyses and magnetic saturation measurements

Fig. 2 shows the DSC curves and the thermal expansion that were obtained during normalization and slow heating. The shape of these curves is typical for the 9%Cr steels [39]. The arrows that point down indicate the occurrence of different transformations. The dilatometric analysis allowed to determine the martensite - start (m_s) and - finish (m_f) temperatures of 375 and 310 °C, respectively, with high accuracy (Fig. 2a) [40]. The determined M_s temperature is similar to that for other 9%Cr steels [19,35]. During heating, a wide exothermic peak, which is associated with a secondary phase precipitation [19,21,41,42], is observed for a wide temperature interval of 290–580 °C (Fig. 2b). Two small peaks at 380 and 485 °C can be distinguished within this large peak. Therefore, the precipitation of two different types of carbides/carbonitrides occurs at these temperatures [19,21,41,42]. The first clearly defined endothermic peak at 745 °C is attributed to the ferromagnetic→paramagnetic transformation of the α-ferrite upon reaching the Curie temperature, T_C [42,43]. Therefore, the T_C value of this steel is 23K lower than the Curie temperature of 768 °C for α-Fe [43]. The second endothermic peak arises from the α→γ transformation onset, which is accompanied by the dissolution of $M_{23}C_6$ carbides. The thermal expansion curve analysis shows that A_{c1} and A_{c3} are 796 and 858 °C, respectively. Furthermore, the corresponding inflection points are observed at 808 and 885 °C on the DSC curve. The third endothermic peak at 978°Cis attributed to the dissolution of secondary phases in austenite. There is no evidence for the α-ferrite+$M_{23}C_6$→γ- austenite transformation [42]. It is likely that the extensive $M_{23}C_6$ dissolution in austenite begins at 938 °C and ends at approximately 990 °C.

The magnetic saturation measurement showed that the retained austenite volume fraction after normalizing is approximately 6%. After tempering at temperatures of 350 and 525 °C, the retained austenite volume fraction decreases to 4% and 2%, respectively. No retained austenite was detected after tempering at 650 °C. Thus, the retained austenite temperature of complete dissolution in the studied steel is higher than in other 9–10%Cr steels [13,21].

3.3. Microstructure

3.3.1. As-normalized condition

The normalizing heat treatment leads to the formation of the typical lath martensite structure with a four-level hierarchy in its morphology, i.e., PAGs (Fig. 3), packets, blocks and laths of martensite [19]. The δ-ferrite was not detected as predicted by Eq. (2). The two types of particles were observed in the martensitic matrix. The first type is the needle-shaped Fe-enriched M_3C cementite with an average longitudinal size of approximately 110 nm. The orientation relationship (OR) between ferrite and cementite described as the Bagaryatski OR [43,44] was found:

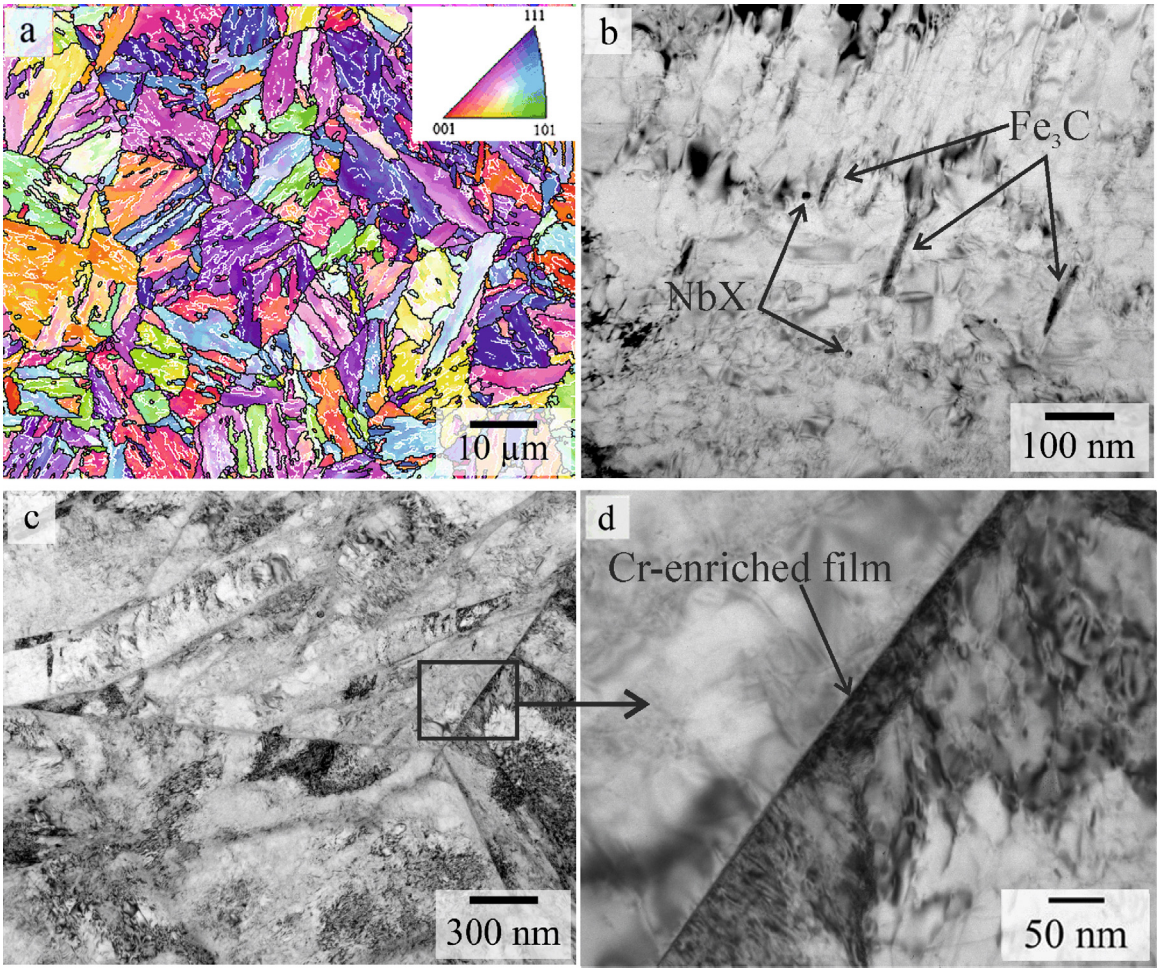

Fig. 3. The microstructure of studied steel after normalization at 1060 °C: OIM micrograph (a), Bright field TEM images (b, c, d).

$$[001]_{Fe_3C} \| [\bar{1}01]_{\alpha-ferrite},$$
$$[100]_{Fe_3C} \| [111]_{\alpha-ferrite},$$
$$[010]_{Fe_3C} \| [\bar{1}2\bar{1}]_{\alpha-ferrite}. \quad (3)$$

This OR appears when cementite precipitates from martensite during tempering [44]. Only one family of cementite platelets is readily distinguished within each lath. This is in contrast with the other 9%Cr steels [41,45], where cementite precipitates from austenite under normalizing and obeys the following OR: $[113]_{Fe3C} \| [111]_{\alpha\text{-ferrite}}$.

The second type of particles are spherical-shaped NbC with an average size of approximately 50 nm (Table 4). In addition, small amount of Ti-enriched MX carbonitrides was detected. The Cr-enriched interlath films or the films located at PAG boundaries with an average width of 5–10 nm were found (Table 4).

3.3.2. *Tempered conditions*

The typical OIM maps and bright field TEM images of tempered steel are shown in Figs. 4 and 5. The structural characteristics and dimensions of the secondary phase particles are summarized in Table 4. Tempering does not significantly affect the lath thickness, which increases to 280 and 300 nm after tempering at temperatures of 500 and 750 °C, respectively. The average distance between high angle boundaries remains unchanged up to the tempering temperature of 500 °C and tends to increase at higher temperatures. The remarkable decrease in lattice dislocation density is observed after tempering at 500 °C. At tempering

Table 4
Effect of tempering temperature on the structural parameters.

Tempering temperature, °C	Normalized	350	500	650	750
Martensitic lath width, nm	250 ± 35	250 ± 30	280 ± 40	280 ± 35	300 ± 50
Dislocation density, $\times 10^{14}$ m^{-2}	5.4 ± 1.2	6.1 ± 1.1	3.8 ± 0.7	2.3 ± 0.5	2.6 ± 0.5
Distance between HABs, μm	2.7 ± 0.5	2.8 ± 0.6	2.5 ± 0.4	3.4 ± 1.1	3.7 ± 1.3
Average width of Cr-enriched films, nm	15 ± 4	23 ± 7	35 ± 13	50 ± 18	–
Average size of globular $M_{23}C_6$, nm	–	–	57 ± 10	64 ± 28	70 ± 25
Average size of VX, nm	–	–	–	–	49 ± 16
Average size of NbX, nm	48 ± 10	42 ± 11	43 ± 13	45 ± 15	47 ± 10
Average size of TiX, nm	–	68 ± 18	78 ± 19	70 ± 12	75 ± 14
Average size of M_3C, nm	110 ± 25	105 ± 20	123 ± 32	–	–

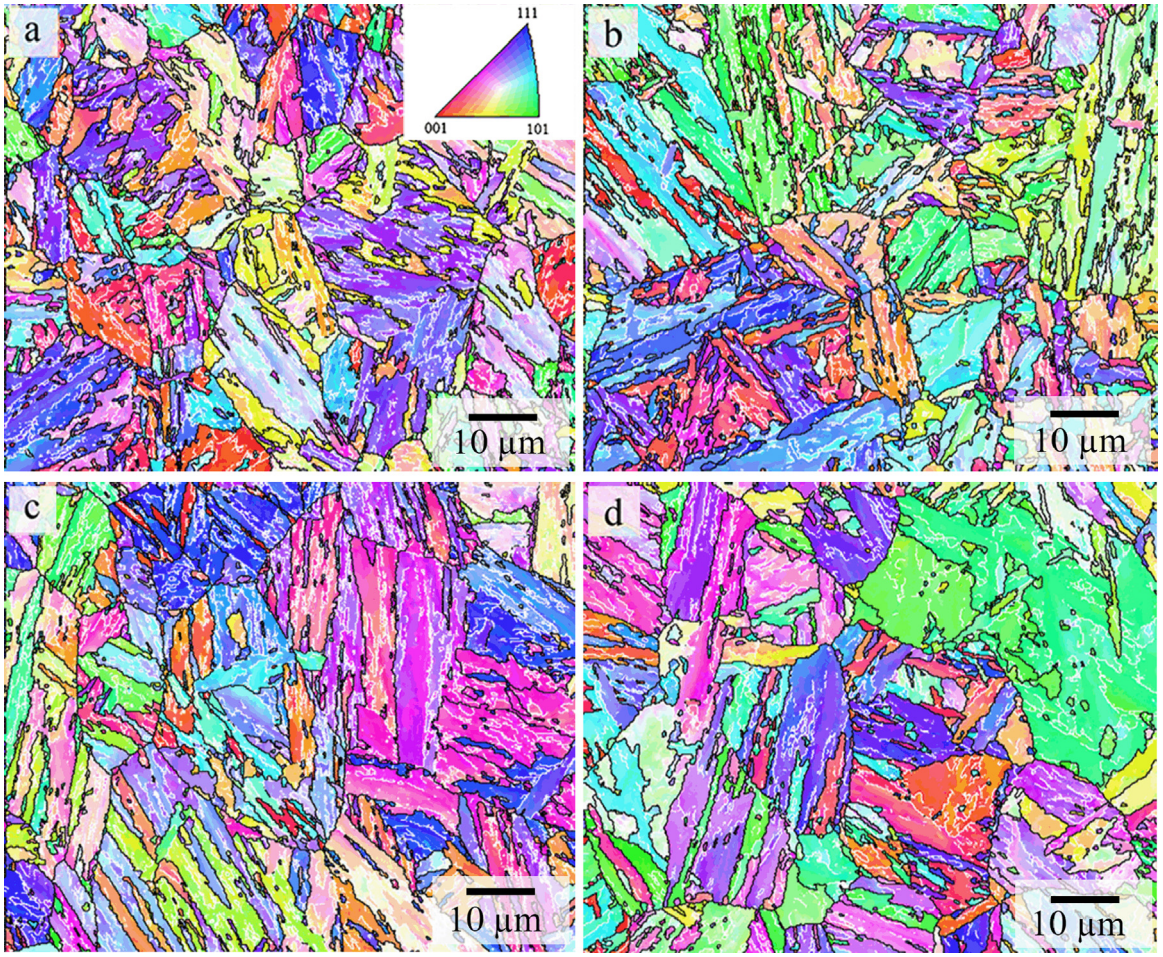

Fig. 4. OIM images after normalization at 1060 °C and tempering at: 350 °C (a), 500 °C (b), 650 °C (c) and 750 °C (d). The black and white lines indicate high-angle (HAB) and low-angle (LAB) boundaries, respectively.

temperatures $\geq$650 °C, the two-fold decrease in the dislocation density is observed in comparison with a normalized condition (Table 4).

No effect of tempering temperature up to 500 °C on the morphology, size and OR of cementite platelets was found (Figs. 6 and 7). Only W-enriched M_3C carbides containing $\leq$10 wt%Cr were detected. After tempering at 350°Cand 500 °C, the two-phase separation of M(C,N) carbonitrides into Nb-enriched particles with an average size of ~42 nm and Ti-enriched particles with anaverage size of ~73 nm takes place. The Nb-enriched M(C,N) carbonitrides contain a small amount of Ti, while the Ti/Nb ratio in the Ti-enriched M(C,N) carbonitridesis ~3.5. It is worth noting that the Nb-enriched M(C,N) carbonitrides located near the Cr-enriched films contain W. The dispersion of these M(C,N) carbonitrides remains unchanged with the further tempering temperature increase up to 750 °C. The broadening of the Cr-enriched films is accompanied by the increase in Cr and W content. These films comprise almost continuous layers. At the tempering temperature of 500 °C, the first $M_{23}C_6$ carbides with an average thickness of ~55 nm and a round shape appear near the Cr-enriched films (Fig. 7). In addition, the film-shaped $M_{23}C_6$ carbides replace the Cr-enriched films. As suggested, these $M_{23}C_6$ carbides do not exhibit any rational orientation relationships with the ferrite matrix (Fig. 8). The average size of the retained Cr-enriched films increases to 35 nm. The chemical composition of the two types of $M_{23}C_6$ carbides with plate-like and film-like shapes is approximately the same.

After tempering at 650 °C, the lath and the block boundary are decorated with $M_{23}C_6$ carbides (Fig. 9). The continuous layers of Cr-enriched films partially disintegrate into chains of $M_{23}C_6$ carbide with a plate-like shape and an average thickness of ~65 nm and the remnants of the Cr-enriched films. No Fe_3C particles were found at this tempering temperature. After tempering at 750 °C, the Cr-enriched films were completely replaced by the $M_{23}C_6$ particles (Fig. 10). Additionally, the selected area diffraction (SAD) patterns (Fig. 11) indicate that $(110)_\alpha$ is parallel to $(111)_{Cr_{23}C_6}$. The following orientation relationships between ferrite and $M_{23}C_6$ after tempering at 750 °C were obtained:

$$(110)_\alpha \| (111)_{Cr_{23}C_6} [1\bar{1}\bar{1}]_\alpha \| (01\bar{1})_{Cr_{23}C_6}$$ Kurdjumov–Sachs

$$(110)_\alpha \| (111)_{Cr_{23}C_6} [00\bar{1}]_\alpha \| [01\bar{1}]_{Cr_{23}C_6}$$ Nishiyama–Wassermann

Therefore, the $M_{23}C_6$ carbides with the KS and NW orientation relationships independently precipitated at the boundaries and grew at the expense of $M_{23}C_6$ carbides exhibited no rational OR.

The spheroidization and coagulation of $M_{23}C_6$ carbides lead to the increase of their average size to ~75 nm, and the $Me_{23}C_6$ carbides acquire a round shape. The V-enriched M(C,N) carbonitrides precipitate in addition to the Nb- and Ti-enriched M(C,N) particles. Most of the V-enriched M(C,N) carbonitrides exhibit an equiaxed shape, and their size is larger than that of Nb-enriched M(C,N). The ratios of V/Nb~6 and Nb/V~10 are observed in the V-and Nb-enriched M(C,N) carbonitrides, respectively. The carbonitrides are homogeneously distributed in the tempered martensitic matrix. Therefore, after tempering at 750 °C, the three-phase separation of

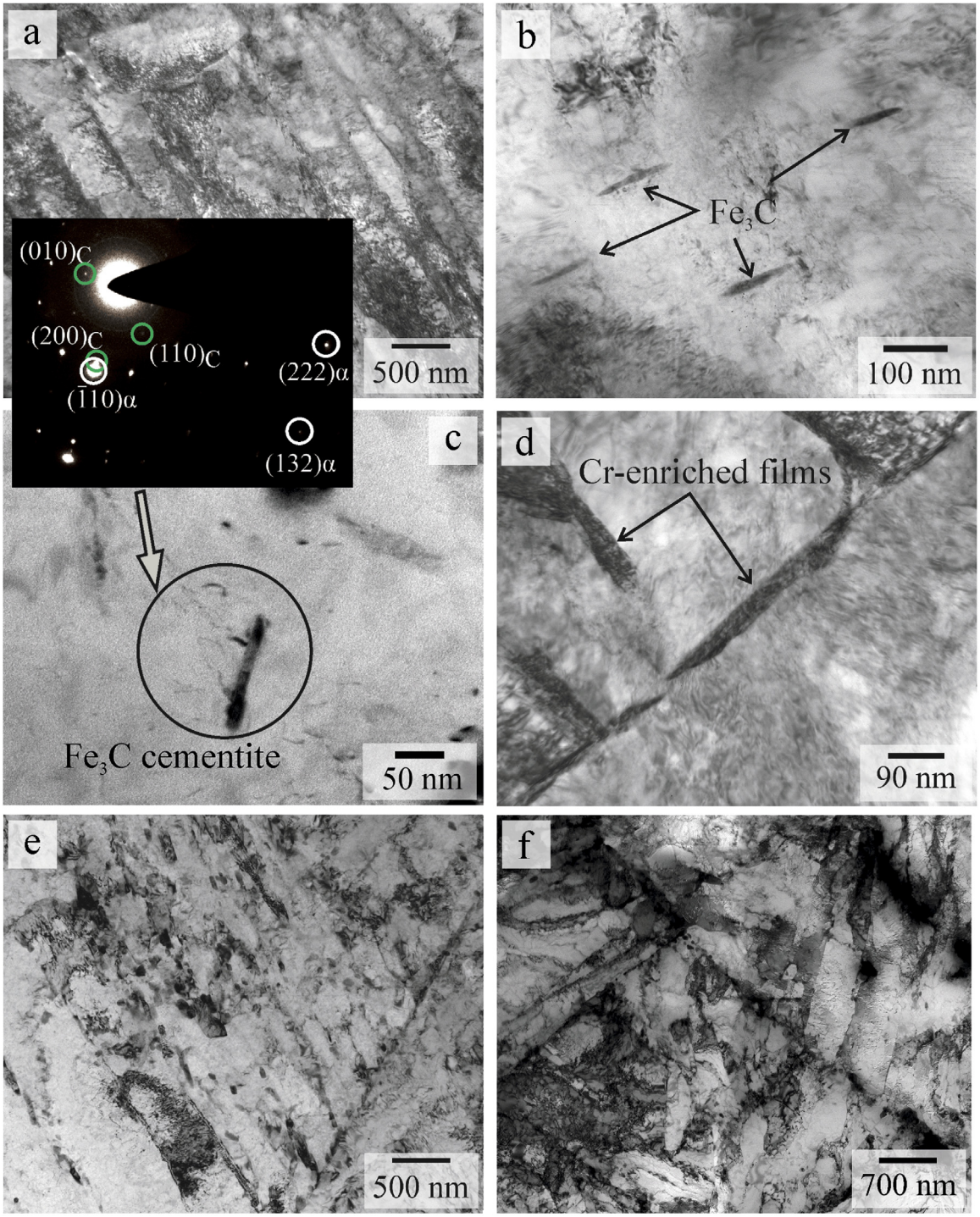

Fig. 5. Bright field TEM images after normalization at 1050 °C and tempering at: 350 °C (a, b, c), 500 °C (d), 650 °C (e) and 750 °C (f).

M(C,N)carbonitrides into V-enriched, Nb-enriched and Ti-enriched particles takes place. In contrast to 9%Cr 0.05%N steels [1], the morphology of these carbonitrides is the same. There is only a small difference in the average size. It is worth noting, that the low density of M(C,N) did not allow to determine their OR.

No Laves phase or W-enriched M_6C carbides [1,19] and BN particles were found after normalizing and further tempering. It appears that three hours of tempering are not sufficient for precipitation of Laves-phase [1,46–48]. No segregation of any elements at the TMLS boundaries were found using elemental mapping of W, Mo and Cr.

3.4. Mechanical properties

Fig. 12 shows the typical engineering stress-strain curves of the specimens which were tempered and tested at the same temperatures. After the pronounced initial strain hardening, the apparent steady state flow is attained. Next, the flow stress continuously decreases until fracture. The temperature increase in this interval shortens the apparent steady state stage. In the 525–700 °C temperature interval the well-defined peak stress appears. The temperature increase decreases the rate of strain softening after this peak. At $T \geq 750$ °C, the peak stress is attained after a very small strain.

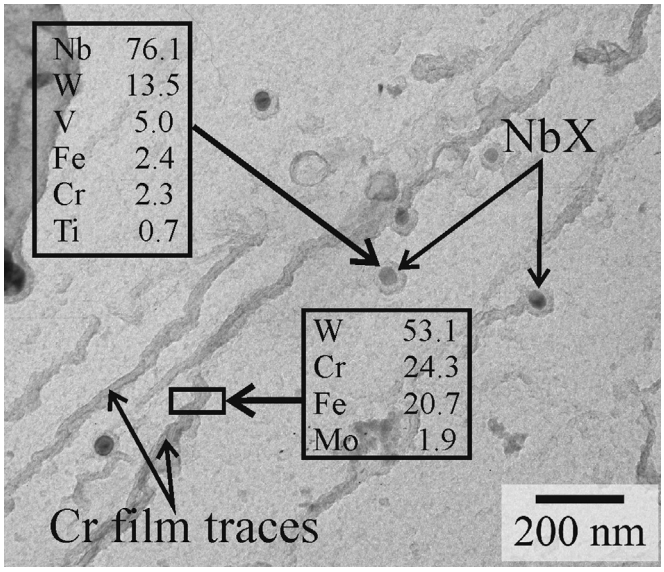

Fig. 6. TEM image of dispersed particles that evolved in the low nitrogen martensitic steel after normalization at 1060 °C and tempering at 350 °C for 3 h. The composition of particles in wt%.

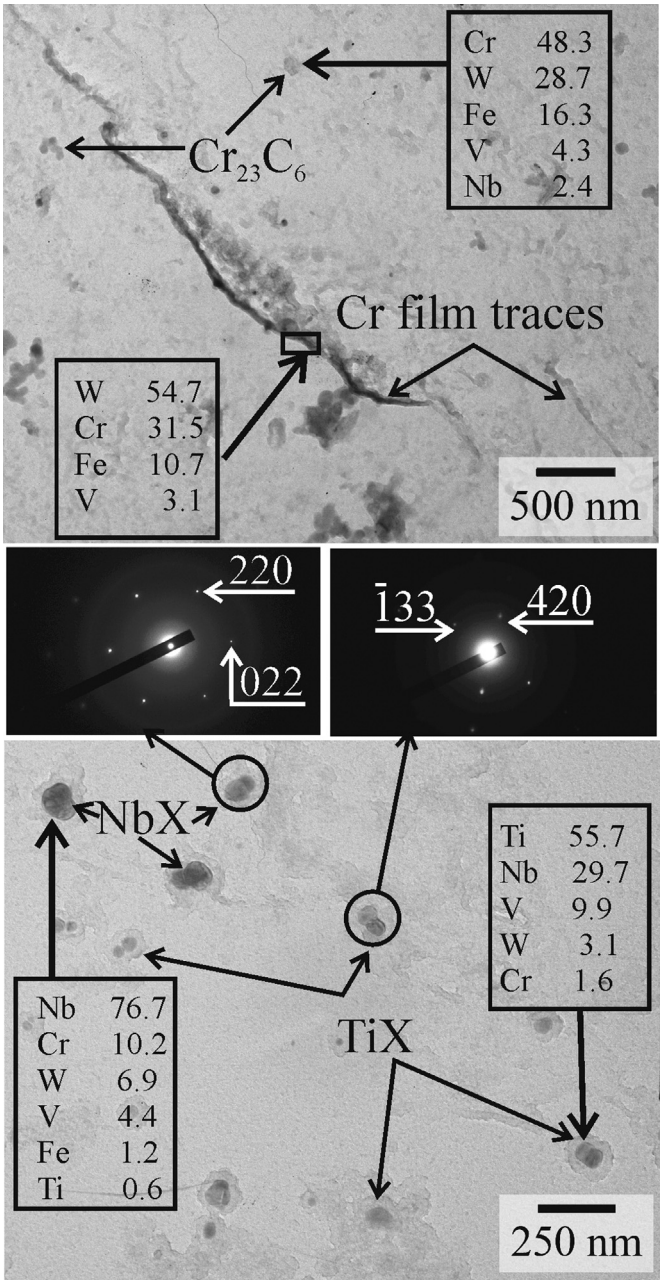

Fig. 7. TEM images of dispersed particles that evolved in the low nitrogen martensitic steel after normalization at 1060 °C and tempering at 500 °C for 3 h. The composition of particles is given in wt%. The circles correspond to the size of the selected-area diffraction.

At temperatures of $T \leq 350$ °C, ductility increases, YS decreases, and UTS remains unchanged with increasing temperatures (Fig. 13 and Table 5). Between 350 °C and 450 °C, the values of YS, UTS and δ are independent of temperature. The UTS and YS values begin to drop at temperatures ≥ 525 °C and ≥ 600 °C, respectively. Ductility decreases when temperature increases from 450 °C to 525 °C, and ductility increases with a further increase in temperature. After tempering at 780 °C, the YS, UTS and δ values are 280 MPa, 290 MPa and 43%, respectively. Thus, no positive temperature dependence on strength [20] was revealed during the entire tempering interval.

Fig. 14 shows the influence of tempering temperature on hardness, impact toughness, ultimate tensile strength (UTS), yield stress (YS), and ductility (δ) at room temperature. The hardness and UTS increase can be interpreted in terms of secondary hardening [44]. However, this increment is three-fold lower than in the 0.05 wt%N containing steel [21]. There is no temperature effect on the shape of σ-ε curves, which are approximately the same, in the samples that are only normalized and in the samples tempered at different temperatures. After tempering at $T \geq 525$ °C, the strain hardening stage is extended, and the uniform elongation shortens. At $T \leq 350$ °C, there is no significant tempering temperature effect on mechanical properties, although the impact toughness slightly increases to~50 J/cm^2, which is a high value for low-temperature-tempered steels [49]. In the temperature interval of 400–500 °C, the hardness, UTS and ductility increase with the tempering temperature increase. The highest values of strength characteristics, such as hardness, YS and UTS, are attained at the tempering temperature of 520 °C. The hardness, YS and UTS increase to 5, 11% and 7%, respectively, in comparison with the normalized condition (Table 5). Simultaneously, the drop of impact toughness to a value of 8.5 J/cm^2 is observed. Upon further tempering temperature increase, the hardness, YS and UTS decrease when the temperature increases. Ductility begins to increase at the tempering temperatures ≥ 580 °C. After tempering at 750 °C, the attained impact toughness is 244 J/cm^2, and the hardness, YS, UTS and ductility values are 236 HB, 590 MPa, 810 MPa and 16%, respectively (Table 5). These values are sufficiently high for the steel to be used without any restrictions attributed to static mechanical properties and fracture toughness [1].

Load-displacement curves (Fig. 15) show very similar loads at an unstable fracture (i.e., maximal load P_M[50]) for all samples except those tempered at 500 °C. After tempering at 500 °C, the P_M value is three-fold lower than at other temperatures. This difference suggests that distinctly different mechanism of unstable crack propagation operates in the samples tempered at 500 °C. The load-displacement curves for the samples subjected to normalization or tempering at 500 °C exhibit a well-defined peak, which indicates the onset of unstable crack propagation immediately after attaining a maximum load, P_M. After tempering at 350 °C, the values of general yield, P_{GY}, maximum load, and P_M [41] are the same. Any evidence for the arrest of crack propagation was not found for the tempering temperatures ≤ 500 °C. However, a well-defined arrest load, P_A, of ~6 kN is observed after tempering at $T \geq 750$ °C. in addition, these tempering temperatures are

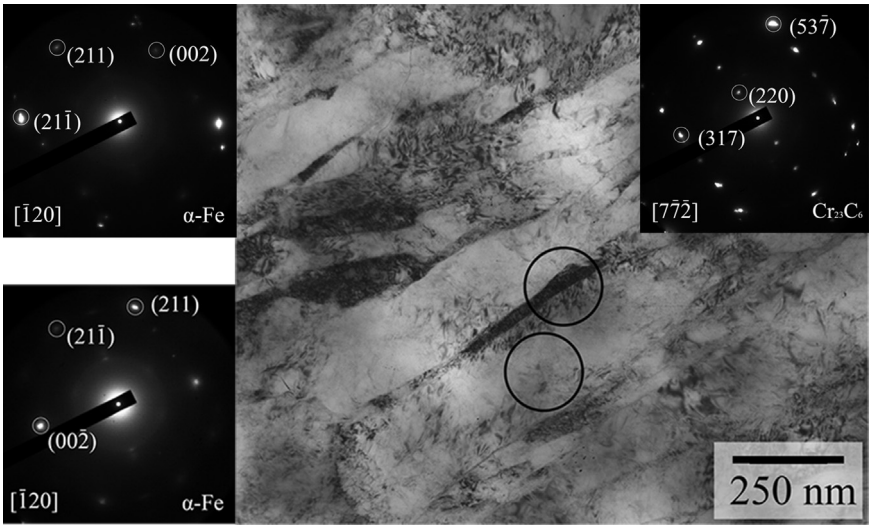

Fig. 8. TEM image of film-shaped $M_{23}C_6$ carbides that evolved after normalization at 1060 °C and tempering at 500 °C for 3 h. The circles correspond to the size of the selected-area diffraction.

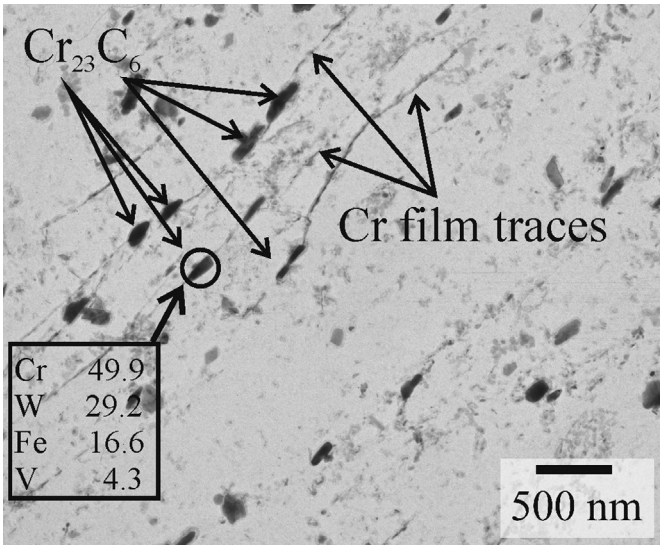

Fig. 9. TEM image of dispersed particles that evolved after normalization at 1060 °C and tempering at 650 °C for 3 h. The composition of particles in wt%.

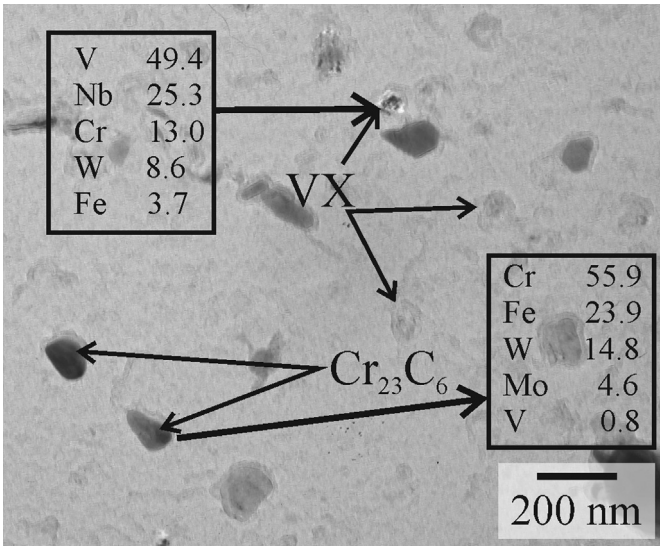

Fig. 10. TEM image of dispersed particles that evolved after normalization at 1060 °C and tempering at 750 °C for 3 h. The composition of particles in wt%.

characterized by the ratio of $P_M/P_{GY} \leq 1.2$. Therefore, the energy is spent forming a ductile crack front that occurs after general yielding. The gradual decrease in the load behind P_M is indicative of a stable crack propagation front.

3.5. Fractography

Fig. 16 shows fracture surface characteristics after impact tests, including the zone of stable crack propagation (SPZ), zone of unstable crack propagation (UPZ) and the zone of arrest of unstable crack (AZ). In the normalizing condition, the stable crack propagation occurs in a mixed brittle-ductile manner with a dominance of quasi-cleavage fracture. The ductile fracture area thickness in SPZ is <0.5 mm. The UPZ occupies more than 90% of overall fracture surfaces. The cleavage facets blend into areas of dimple rupture, and the cleavage steps become tear ridges. The quasi-cleavage fracture primarily occurs through a transgranular path. Rare dimples that are located in a martensitic matrix are shallow and round. The fine and deep dimples are observed at tear ridges. The shallow dimples are observed in AZ, but their portion is not high. Tempering at 350 °C slightly increases the portion of ductile fractures and expands the areas of SPZ and AZ. The stable to unstable crack propagation transition is well distinguishable by the ductile to quasi-cleavage fracture surface transition due to increasing dimple dimensions in a wide transition zone of ~100 μm. The arrest of unstable cracks occurs by increasing the portion of ductile fractures.

The six-fold decrease in the Charpy V-notch impact absorption energy when the tempering temperature increases from 350 °C to 500 °C can be attributed to the complete disappearance of AZ, the ductile/quasi-cleavage fracture SPZ reduction to ~100 μm, and the increasing fraction of intergranular path of crack propagation in UPZ. A stable crack propagation occurs in a nearly ductile manner, and the fracture surface exhibits large shallow dimples. In the UPZ, the quasi-cleavage fracture occurs in a transgranular manner, and the "canyons" that appear along some boundaries are the evidence for intergranular path for crack propagation. After tempering at 650 °C, the arrest of unstable cracks occurs by transition from quasi-cleavage to ductile fracture with dimples exhibiting various sizes. In the AZ, the coarse particles located at the bottom of large dimples serve as void-nucleating sites. After tempering at $T \geq 750$ °C, the UPZ becomes narrow. The crack initiation process

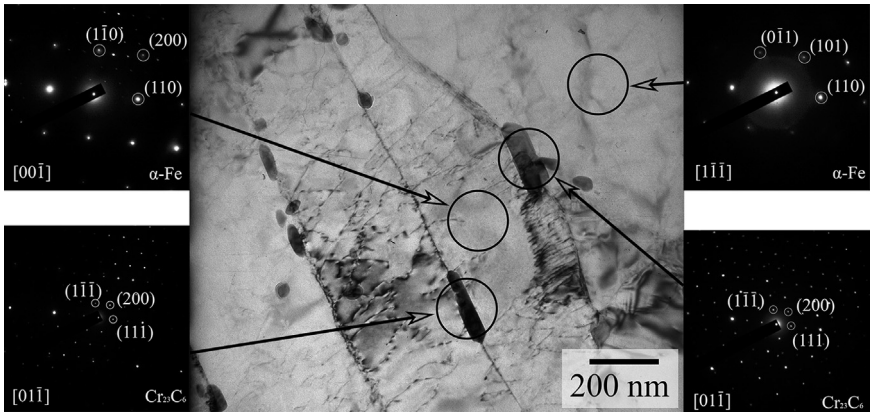

Fig. 11. TEM image of $M_{23}C_6$ carbides that evolved after normalization at 1060 °C and tempering at 750 °C for 3 h. The circles correspond to the size of the selected-area diffraction.

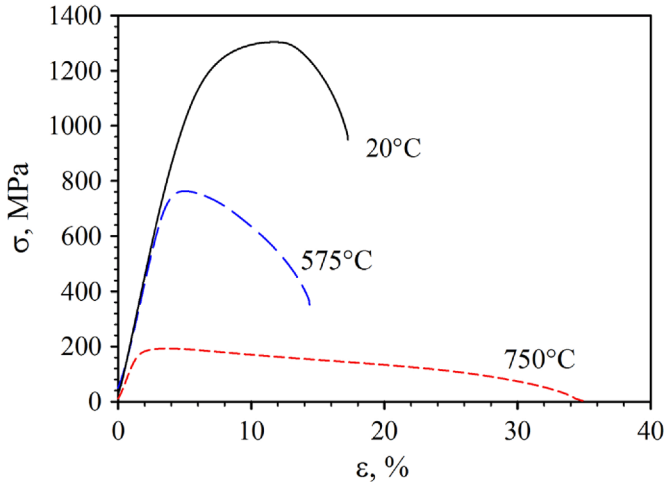

Fig. 12. Experimental engineering stress-strain curves after different tempering/test temperatures.

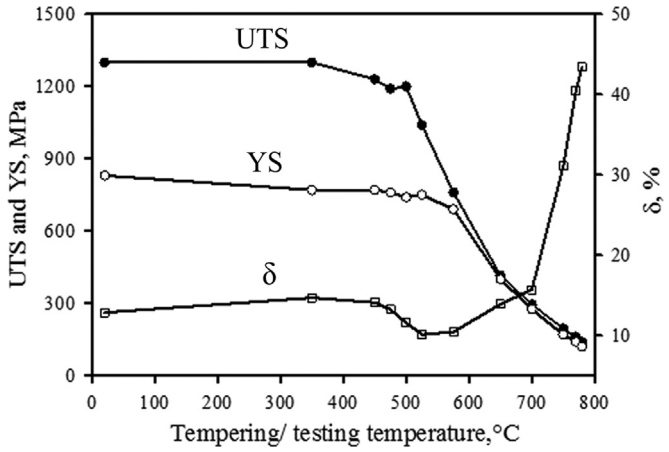

Fig. 13. Effect of tempering temperature on the tensile properties (UTS, YS, ductility). Tests were carried out at tempering temperatures.

produces several cracks that primarily propagate in a ductile manner, and shallow dimples exhibit various dimensions (Fig.16s). It is worth noting, that in UPZ the crack propagation occurs essentially through transgranular path and intergranular fracture plays a minor role. In the AZ, the uniform small dimples are observed (Fig.16t).

4. Discussion

4.1. Precipitation behavior

The precipitation sequence of the present steel can be summarized as follows:

$$\text{Martensite} \rightarrow M_3C \rightarrow M_{23}C_6 \text{ films/round shape} \quad (4)$$

The increase of the B content from 70 [19] to 120 ppm suppresses the segregation of W on PAG and martensitic lath boundaries [35]. The W-enriched M_6C carbides and the Fe_2W phase were not observed. Instead, W contents transient cementite and equilibrium $M_{23}C_6$ carbides are larger than what was predicted by Thermocalc calculations. Cementite precipitates during normalization or annealing. It appears that the $M_{23}C_6$ carbides develop in-situ at the Cr-enriched boundary films and exhibit a direct transformation. That is why no clear orientation relationship between $M_{23}C_6$-type carbides [51] and a ferritic matrix was observed. The absence of regular OR is indicative of the incoherent nature of $M_{23}C_6$/ferrite interfaces. Carbides with such interfaces are highly susceptible to the Ostwald repining, and the size of $M_{23}C_6$-type carbides after high temperature tempering is approximately two-fold higher in comparison with 10 wt%Cr steel [13].

Three-phase separation of M(C,N) carbonitrides appears at high tempering temperature in the 9Cr-3Co-2W-VNbB steel. The following precipitation sequence can be summarized as follows:

$$\begin{aligned}\text{Martensite} &\rightarrow \text{Nb–enriched M(C, N)} + \text{Ti–enriched M(C, N)} \\ &\rightarrow \text{Nb–enriched M(C, N)} + \text{Ti–enriched M(C, N)} + \text{V} \\ &\quad \text{–enriched M(C, N)}\end{aligned} \quad (5)$$

The Nb- and Ti-enriched M(C,N)carbonitrides precipitate under low temperature tempering. It is known that dislocations serve as nucleation sites for these particles [52,53]. The V-enriched M(C,N) carbonitrides precipitate homogeneously under high temperature tempering. Therefore, tempering at $T \geq 650$ °C has no effect on the size and portion of Nb-enriched and Ti-enriched M(C,N) carbonitrides [54]. These three phases are thermodynamically stable, and their particles have nearly the same size and morphology.

Thus, the precipitation process in low N and B-added steel is different compared with the 9%Cr 0.05 wt%N-containing steels [21,55]. A dispersion of secondary phases causes an approximately 25% decrease in lath thickness after tempering at 750 °C, and the effect of decreased N and increased B on dislocation density is insignificant [21,35].

Table 5
Effect of tempering temperature on mechanical properties.

Tempering temperature, °C	Normalized	350	500	650	750
Hardness, HB	377 ± 2	373 ± 2	395 ± 9	281 ± 3	254 ± 5
Impact toughness, J/cm^2	43	54	9	96	244
YS, MPa	830	880	920	680	590
UTS, MPa	1300	1270	1390	890	810
δ, %	12.8	13.2	14.8	14.6	15.9

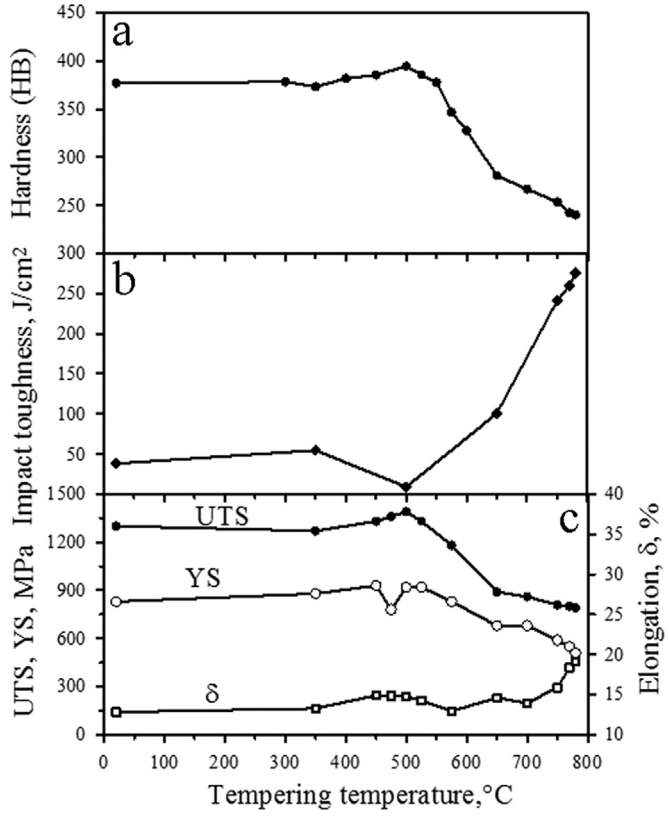

Fig. 14. Effect of tempering temperature on the hardness (a), impact toughness (b), tensile properties (UTS, YS, ductility) (c). Tests were carried out at room temperature.

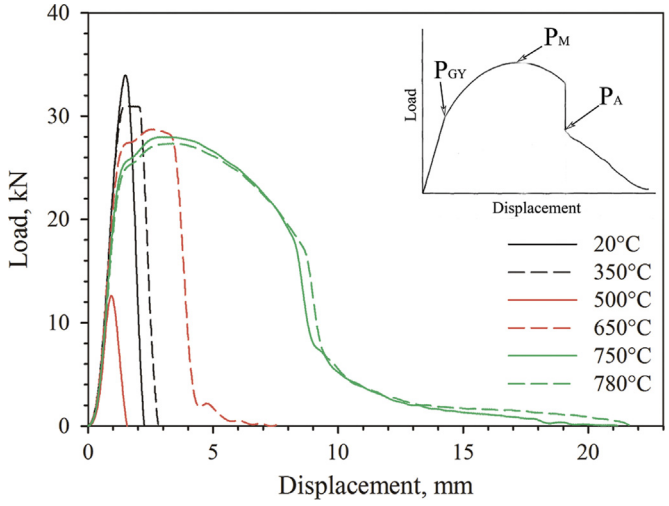

Fig. 15. Experimental load-displacement curves after different tempering temperatures.

4.2. Mechanical and fracture behavior

The 9%Cr steel with 120 ppm of B exhibits good toughness because the BN-free microstructure was achieved using the ratio of B/N = 1.7. No annealing at T ≥ 1150 °C is necessary to prevent the precipitation of coarsened BN inclusions [17]. Embrittlement during tension was not observed. However, after tempering, unstable crack propagation under impact tests takes place. After low temperature tempering, this propagation occurs in a quasi-cleavage manner that provides impact toughness higher than in a hardened 4340 steel [49]. The well-defined tempered martensite embrittlement takes place at ΔT = 150 K higher than in low alloy steels. This is associated with an intergranular fracture [43,44,49]. In this study, the tempered martensite embrittlement is attributed to the three-fold increase in the load for unstable crack propagation due to the formation of boundary $M_{23}C_6$ films instead of the retained austenite, which is located at the interlath or PAG boundaries. The spheroidization and coagulation of $M_{23}C_6$ carbides hinder the unstable crack propagation. The high impact toughness is achieved due to expanding SPZ and AZ.

The decrease of the nitrogen content in the chemical composition of 9%Cr steels from 0.05 to 0.007 wt% significantly diminishes secondary hardening at the tempering temperature of 500 °C.

5. Conclusions

The following tempering behavior features of the 9%Cr steel containing 70 ppm N and 120 ppm of B can be summarized:

1. The 9% Cr steel containing 70 ppm of N and 120 ppm of B exhibits the following precipitation sequence during tempering:
   Martensite → M_3C → $M_{23}C_6$ films/round shape
   Cementite is enriched by W precipitates during auto-tempering and low-temperature tempering. The $M_{23}C_6$ films located at interlath and prior austenite grain boundaries replace the Cr-enriched films at 500 °C, which leads to the tempered martensite embrittlement. Spheroidization and coagulation of these carbides eliminate the embrittlement and provide the Charpy V-notch impact absorption energy of 244 J/cm^2.
2. Heat treatment induces three-phase separation of M(C,N) carbonitrides into Nb-, Ti- and V-enriched particles. The precipitation of Nb- and Ti-enriched M(C,N)carbontrides occurs under auto-tempering and low-temperature tempering, while V-enriched M(C,N)carbonitrides appear under high-temperature tempering. All three carbonitride particle types have round shapes, and their sizes range from 50 nm for Nb- and V-enriched M(C,N) to 75 nm for Ti-enriched M(C,N).
3. The low-temperature-tempered steel exhibits a relatively high toughness of 50 J/cm^2. The tempered martensite embrittlement is attributed to the facilitation of unstable crack propagation, which primarily occurs intransgranular manner. The high

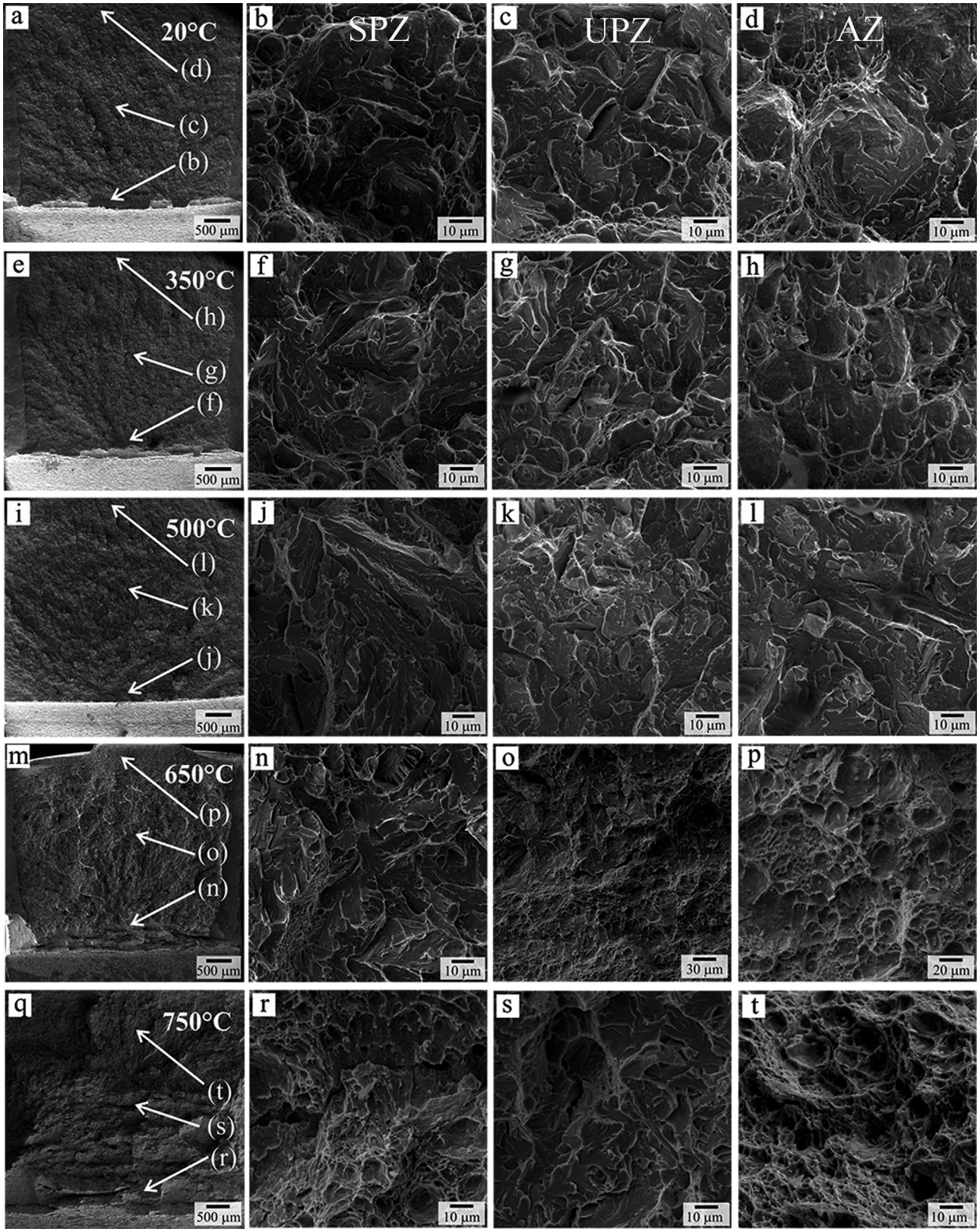

Fig. 16. SEM images of the fractured surface after normalization at 1060 °C (a-d) followed by tempering at: 350 °C (e-h), 500 °C (i-l), 650 °C (m-p) and 750 °C (q-t).

impact toughness after high temperature tempering is associated with the expanded zone of stable crack propagation and the arrest of unstable cracks.

Acknowledgments

The study was financial supported by the Russian Science Foundation, under Grant no. 14-29-00173. The authors are grateful to the staff of the Joint Research Center, Belgorod State University,

for their assistance with instrumental analyses.

References

[1] F. Abe, T.U. Kern, R. Viswanathan, Creep-Resistant Steels, England, 2008.
[2] R.O. Kaybyshev, V.N. Skorobogatykh, I.A. Shchenkova, Phys. Met. Metall. 109 (2010) 200–212.
[3] M. Yoshizawaa, M. Igarashi, K. Moriguchi, A. Iseda, H. Gh Armaki, K. Maruyama, Mater. Sci. Eng. A 510–511 (2009) 162–168.
[4] K. Kimura, H. Kushima, K. Sawada, Mater. Sci. Eng. A 510–511 (2009) 58–63.
[5] R.O. Kaibyshev, V.N. Skorobogatykh, I.A. Shchenkova, Met. Sci. Heat. Treat. 52 (2010) 90–99.
[6] H.K. Danielsen, J. Hald, Mater. Sci. Eng. A 505 (2009) 169–177.
[7] L. Cipolla, H.K. Danielsen, D. Venditti, P.E. Di Nunzio, J. Hald, M.A.J. Somers, Acta Mater. 58 (2010) 669–679.
[8] J. Hald, Int. J. Press. Vessel. Pip. 85 (2008) 30–37.
[9] H. Semba, F. Abe, Energy Mater. 1 (2006) 238–244.
[10] M. Tabuchi, H. Hongo, F. Abe, Metal. Mater. Trans. A 45 (2014) 5068–5075.
[11] Y. Liu, S. Tsukamoto, K. Sawada, F. Abe, Metal. Mater. Trans. A 45 (2014) 1306–1314.
[12] Y. Liu, S. Tsukamoto, K. Sawada, M. Tabuchi, F. Abe, Metal. Mater. Trans. A 46 (2015) 1843–1854.
[13] N. Dudova, R. Mishnev, R. Kaibyshev, ISIJ Int. 51 (2011) 1912–1918.
[14] S. Albert, M. Kondo, M. Tabuchi, F. Yin, K. Sawada, F. Abe, Metall. Mater. Trans. A 36 (2005) 333–343.
[15] C.R. Das, S.K. Albert, A.K. Bhaduri, B.S. Murty, Metal. Mater. Trans. A 42 (2011) 940–951.
[16] A. Golpayegani, F. Liu, H. Svensson, M. Andersson, H.-O. Andren, Metal. Mater. Trans. A 44 (2013) 2171–2186.
[17] L. Li, R. Maclachlan, M.A.E. Jepson, R. Thomson, Metal. Mater. Trans. A 44 (2013) 3411–3418.
[18] K. Sakuraya, H. Okada, F. Abe, Energy Mater. 1 (2006) 158–166.
[19] N. Dudova, R. Kaibyshev, ISIJ Int. 51 (2011) 826–831.
[20] H. Kitahara, R. Ueji, N. Tsuji, Y. Minamino, Acta Mater. 54 (2006) 1279–1288.
[21] A. Yu Kipelova, A.N. Belyakov, V.N. Skorobogatykh, I.A. Shchenkova, R. O. Kaibyshev, Metal. Sci. Heat. Treat. 52 (2010) 100–110.
[22] I. Fedorova, Z. Yanushkevich, A. Belyakov, R. Kaibyshev, Adv. Mater. Res. 409 (2012) 672–677.
[23] N. Dudova, A. Plotnikova, D. Molodov, A. Belyakov, R. Kaibyshev, Mater. Sci. Eng. A 534 (2012) 632–639.
[24] V. Dudko, A. Belyakov, D. Molodov, R. Kaibyshev, Metall. Mater. Trans. A 44 (2013) 162–172.
[25] I. Fedorova, A. Kipelova, A. Belyakov, R. Kaibyshev, Metall. Mater. Trans. A 44 (2013) 128–135.
[26] A. Kostka, K.G. Tak, R.J. Hellmig, Y. Estrin, G. Eggeler, Acta Mater. 55 (2007) 539–550.
[27] Lakshmiprasad Maddi, A.R. Ballal, D.R. Peshwe, R.K. Paretkar, K. Laha, M. D. Mathew, Mater. Sci. Eng. A 639 (2015) 431–438.
[28] V. Sklenička, K. Kuchařová, P. Král, M. Kvapilová, M. Svobodová, J. Čmakal, Mater. Sci. Eng. A 644 (2015) 297–309.
[29] T. Sakthivel, S. PanneerSelvi, K. Laha, Mater. Sci. Eng. A 640 (2015) 61–71.
[30] F. Abe, Mater. Sci. Eng. A 510–511 (2009) 64–69.
[31] F. Lu, P. Liu, H. Ji, Y. Ding, X. Xu, Y. Gao, Mater. Charact. 92 (2014) 149–158.
[32] R.K. Shiue, K.C. Lan, C. Chen, Mater. Sci. Eng. A 287 (2000) 10–16.
[33] P.B. Hirsch, A. Howie, R.B. Nicholson, et al., Electron Microscopy of Thin Crystals, second ed, Krieger, New York, 1977.
[34] K. Suzuki, S. Kumai, Y. Toda, H. Kushima, K. Kimura, ISIJ Int. vol. 43, 2003, pp. 1089–1094.
[35] A. Fedosseva, N. Dudova, R. Kaibyshev, Mater. Sci. Eng. A 654 (2016) 1–12.
[36] V. Knezevic, J. Balun, G. Sauthoff, G. Inden, A. Schneider, Mater. Sci. Eng. A 477 (2008) 334–343.
[37] P. Mayr, T.A. Palmer, J.W. Elmer, E.D. Specht, S.M. Allen, Metall. Mat. Trans. A 41 (2010) 2462–2465.
[38] S.H. Ryu, J. Yu, Metall. Mater. Trans. A 29 (1998) 1573–1578.
[39] T. Tokunagaa, K. Hasegawab, F. Masuyama, Mater. Sci. Eng. A 510–511 (2009) 158–161.
[40] H.-S. Yang, H.K.D.H. Bhadeshia, Mater. Sci. Technol. 23 (2007) 556–560.
[41] Ch Liu, D. Zhang, Y. Liu, Q. Wang, Z. Yan, Nucl. Eng. Des. 241 (2011) 2411–2415.
[42] B.J. Ganesh, S. Raju, A.K. Rai, E. Mohandas, M. Vijayalakshmi, K.B.S. Rao, B. Raj, Mater. Sci. Technol. 27 (2011) 500–512.
[43] Bruno C. De Cooman, John G. Speer, Fundamentals of Steel Product Physical Metallurgy, Association for Iron & Steel Technology, 2011.
[44] H.K.D.H. Bhadeshia, R. Honeycombe, Steels: Microstructure and Properties, third ed, Butterworth-Heinemann, UK, 2006.
[45] L.-Q. Xu, D.-T. Zhang, Y.-Ch Liu, B.-Q. Ning, Zh-X. Qiao, Z.-Sh Yan, H.-J. Li, Int. J. Miner. Metall. Mater. 21 (2014) 438–447.
[46] M.I. Isik, A. Kostka, V.A. Yardley, K.G. Pradeep, M.J. Duarte, P.P. Choi, D. Raabe, G. Eggeler, Acta Mater. 90 (2015) 94–104.
[47] I. Fedorova, A. Belyakov, P. Kozlov, V. Skorobogatykh, I. Shenkova, R. Kaibyshev, Mater. Sci. Eng. A 615 (2014) 153–163.
[48] G. Chakraborty, C.R. Das, S.K. Albert, A.K. Bhaduri, V. Thomas Paul, G. Panneerselvam, A. Dasgupta, Mater. Charact. 100 (2015) 81–87.
[49] G. Krauss, Metall. Mater. Trans. A 32 (2001) 861–877.
[50] ASM Handbook, Mechanical Testing and Evaluation, vol. 8, ASM International Materials Park, OH, 2000.
[51] A. Kipelova, A. Belyakov, R. Kaibyshev, Philos. Mag. 93 (2013) 2259–2268.
[52] F. Perrard, A. Deschamps, P. Maugis, Acta Mater. 55 (2007) 1255–1266.
[53] C. Hin, Y. Brechet, P. Maugis, F. Soisson, Acta Mater. 56 (2008) 5535–5543.
[54] Y.Zh Shen, S.Ho Kim, H.D. Cho, Ch.H. Han, W.S. Ryu, J. Nucl. Mater. 400 (2010) 94–102.
[55] C. Hurtado-Norena, C.A. Danon, M.I. Luppo, P. Bruzzoni, Metall. Mater. Trans. A 46 (2015) 3972–3988.